

Scanning Confocal Electron Energy-Loss Microscopy Using Valence-Loss Signals

Huolin L. Xin,^{1,*} Christian Dwyer,² David A. Muller,^{3,4} Haimei Zheng,¹ and Peter Ercius^{5,*}

¹Materials Sciences Division, Lawrence Berkeley National Lab, Berkeley, CA 94720, USA

²Monash Centre for Electron Microscopy, ARC Centre of Excellence for Design in Light Metals, Department of Materials Engineering, Monash University, Clayton, Vic. 3800, Australia

³School of Applied and Engineering Physics, Cornell University, Ithaca, NY 14850, USA

⁴Kavli Institute at Cornell for Nanoscale Science, Cornell University, Ithaca, NY 14850, USA

⁵National Center for Electron Microscopy, Lawrence Berkeley National Lab, Berkeley, CA 94720, USA

Abstract: Finding a faster alternative to tilt-series electron tomography is critical for rapidly evolving fields such as the semiconductor industry, where failure analysis could greatly benefit from higher throughput. We present a theoretical and experimental evaluation of scanning confocal electron energy-loss microscopy (SCEELM) using valence-loss signals, which is a promising technique for the reliable reconstruction of materials with sub-10-nm resolution. Such a confocal geometry transfers information from the focused portion of the electron beam and enables rapid three-dimensional (3D) reconstruction by depth sectioning. SCEELM can minimize or eliminate the missing-information cone and the elongation problem that are associated with other depth-sectioning image techniques in a transmission electron microscope. Valence-loss SCEELM data acquisition is an order of magnitude faster and requires little postprocessing compared with tilt-series electron tomography. With postspecimen chromatic aberration (C_c) correction, SCEELM signals can be acquired in parallel in the direction of energy dispersion with the aid of a physical pinhole. This increases the efficiency by $10\times$ – $100\times$, and can provide 3D resolved chemical information for multiple core-loss signals simultaneously.

Key words: scanning confocal electron energy-loss microscopy, inelastic confocal, aberration-corrected electron microscopy, chromatic aberration correction

INTRODUCTION

Aberration-corrected scanning transmission electron microscopy (STEM) can now routinely provide images and spectroscopic information at atomic resolution (Batson et al., 2002; Bosman et al., 2007; Muller et al., 2008; Muller, 2009; Botton et al., 2010; Kourkoutis et al., 2010; Tan et al., 2011; Xin et al., 2011). However, in a scanning transmission electron microscope, the sample is viewed in projection, and the structural variations along the incident beam direction cannot be fully determined from a single image. Annular dark-field and incoherent bright-field STEM (ADF-STEM and IBF-STEM) tomography, which operate in a similar manner to a medical CAT scan, allow for three-dimensional (3D) reconstruction of structures from a series of images recorded at multiple orientations (Midgley & Weyland, 2003; Ercius et al., 2006; Li et al., 2009; Midgley & Dunin-Borkowski, 2009). Although electron tomography has proven successful for materials applications, it usually requires 1–6 h to acquire a tilt series and possibly days to process the projections into 3D tomograms. Thus, this technique is not sufficiently efficient for real-time quality control and failure analysis, as required, for example, by the semiconductor industry. Therefore, it is desirable to find a faster alternative to electron tomography with comparable resolution. In this paper, we demonstrate that scanning confocal electron energy-loss

microscopy (SCEELM) using low-energy-loss signals can reconstruct samples with nanometer-sized depth resolution. This method has a dose efficiency comparable to that of ADF-STEM depth sectioning and bright-field scanning confocal electron microscopy (BF-STEM), but the efficiency can be increased by $10\times$ – $100\times$ with postspecimen C_c correction by the parallel acquisition of SCEELM signals in the spectroscopy mode (Fig. 1c). This technique is free of the missing-information cone and elongation artifacts that are characteristic of transmission electron microscopy (TEM) tomography and has the potential to enable rapid and reliable 3D reconstruction of materials with sub-10-nm depth resolution in current state-of-the-art transmission electron microscopes. This paper also highlights the ramifications of postspecimen C_c correction in confocal applications (Figs. 1b, 1c).

The development of aberration-correcting electron optics has greatly increased the available numerical apertures of STEMs, leading to smaller electron probes with higher beam current (Krivanek et al., 2003). Whereas lateral resolution varies inversely proportional to the first power of the numerical aperture, the depth of focus of a convergent beam undergoes a more rapid scaling with aperture size (Born & Wolf, 1999). The depth of focus has improved from ~ 50 nm in a conventional instrument to ~ 5 nm in an aberration-corrected STEM (Cosgriff et al., 2008; Xin & Muller, 2009, 2010). This may enable ADF-STEM to localize dopant atoms in amorphous matrices and in crystals if

Received June 10, 2012; accepted March 27, 2013

*Corresponding author. E-mail: hxin@lbl.gov; percius@lbl.gov

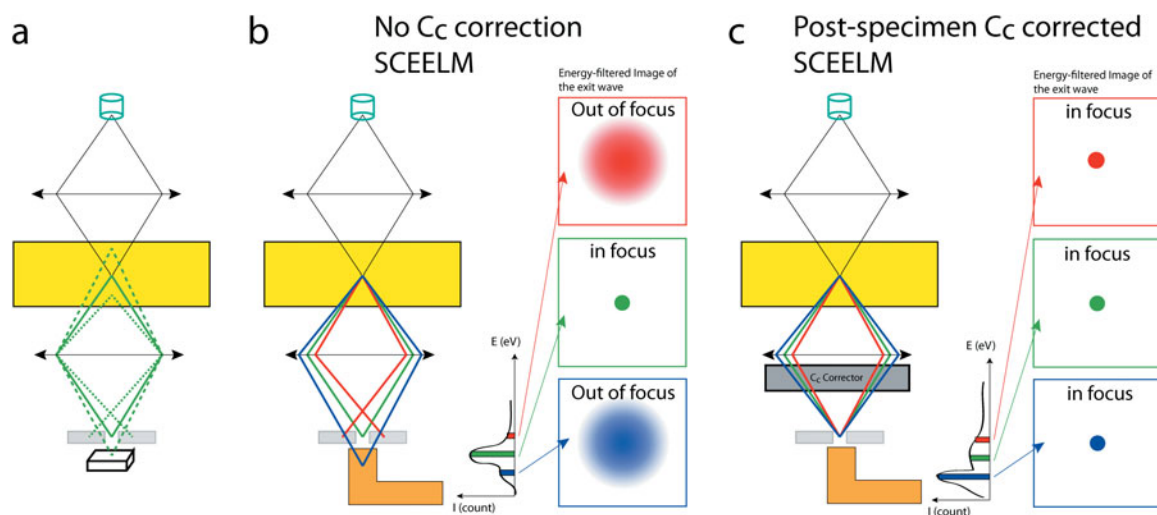


Figure 1. Schematics for scanning confocal electron energy-loss microscopy (SCEELM). **a:** A typical optical confocal microscope setup where the single-wavelength green fluorescence signal is focused. The in-focus signal is collected by an area detector behind the pinhole and the out-of-focus signals are mostly blocked. **b:** A typical SCEELM setup in a double-corrected transmission electron microscopy (TEM) without postspecimen C_c correction. Exit waves with different energies are not simultaneously in focus. This setup only allows one energy loss to be used at a time. (The image of the exit waves are drawn as if the pinhole is not used.) **c:** SCEELM setup in a C_c corrected TEM. Exit waves in a wide energy window are simultaneously in focus. In spectroscopy mode, with the aid of a pinhole, SCEELM signals at different energy losses can be recorded in parallel. Unlike scanning transmission electron microscopy-electron energy-loss spectroscopy (STEM-EELS), the collected EELS spectra do not reflect the projected chemical structure of the materials but the volumes selected by the crossover of the beam.

channeling can be sufficiently suppressed (Xin et al., 2008a, 2008b; Couillard et al., 2011), but determining depth information of extended objects by simply varying the focus has proven challenging and is prone to artifacts (Xin & Muller, 2009). Despite the short depth of focus, the 3D contrast transfer function (CTF) of ADF-STEM has a large missing-information cone where the opening angle of information transfer is equal to the probe-forming angle. This results in severe elongation of reconstructions of extended objects from focal-series (D'Alfonso et al., 2008; Intaraprasong et al., 2008; Xin & Muller, 2009; Hashimoto et al., 2012) by factors of approximately $20\times$ – $40\times$ in current aberration-corrected instruments. Such a large elongation can result in unexpected artifacts, such as the appearance of a small feature within a larger one in the reconstruction of an object where the smaller feature is located outside of the larger one (Xin & Muller, 2009). The root of the problem is that the total intensity of the out-of-focus blur is identical to that of the in-focus image. In hopes of improving depth discrimination, postspecimen lenses have been exploited to form a confocal geometry to reject the blurred information from out-of-focus electrons (Frigo et al., 2002; Einspahr & Voyles, 2006). However, it was found that BF-STEM using elastic signals suffers from the same missing-information cone and elongation artifacts of conventional tomography (Takeguchi et al., 2008; Xin & Muller, 2009, 2010; Mitsuishi et al., 2010; Hashimoto et al., 2011; Wang et al., 2011).

Bright-field confocal laser scanning microscopy (the optical counterpart of BF-STEM) also suffers from the missing-information cone problem (Streibl, 1985; Shep-

pard, 1986a, 1986b; Hashimoto et al., 2011), but is minimized by using a high numerical aperture close to one. Optically, the missing-information cone can be eliminated by using the fluorescence and Raman signals (Sheppard & Choudhury, 1977; Sheppard, 1986b) (Fig. 1a), which also nearly doubles the lateral and depth resolution of a fluorescence/Raman microscope relative to its elastic counterpart (Cox et al., 1982). Similar signals are present in TEM. X-ray emissions in TEM, the counterpart of fluorescence signals in optical confocal microscopy, could potentially be used. However, the current technology for focusing soft and hard X-rays is still premature for a broad-spectrum application in a TEM; this technology may become relevant in the future in response to the need for the ability to focus high-brightness X-rays in fourth-generation light sources.

Despite the lack of intermediate transition states, the counterpart in TEM of Raman signals in optical confocal microscopy in this case is electron energy-loss spectroscopy (EELS). STEM using electron energy-loss signals has been proposed in previous studies (D'Alfonso et al., 2008; Xin & Muller, 2009), and theoretical simulations demonstrated that core-loss SCEELM has an improved depth discrimination compared with BF-STEM and ADF-STEM. The concept of core-loss SCEELM was experimentally verified by Wang and colleagues using the carbon K edge ($1s \rightarrow 2p$ and continuum) on a carbon thin film (Wang et al., 2010). They demonstrated that the core-loss confocal signal decreases as the thin film moves away from the focused electron probe, whereas the ADF-STEM intensity remains constant. For this technique, energy-filtered images of the electron probe must

be recorded in series, and the defocus must be readjusted for each different energy loss due to the large chromatic aberration $C_c \sim 1\text{--}2$ mm of the postspecimen lenses (see Fig. 1b). Thus, the dose efficiency of SCEELM is limited by C_c and is comparable to that of energy-filtered TEM. We show that a postspecimen C_c corrector and a physical pinhole allow SCEELM signals to be recorded in parallel, making it comparable to STEM-EELS in collection efficiency (Fig. 1c).

The relative intensity of core-loss inelastic signals of major edges within 100–1,500 eV are approximately three to four orders of magnitude smaller than the elastic signal. Conceptually, core-loss SCEELM can be applied to the 3D reconstruction of elemental distributions of the probed specimen, but this is difficult in practice. A large fraction of the inelastically scattered signal is in the valence-EELS region (5–50 eV energy loss), and could provide a $100\times\text{--}1,000\times$ improvement in dose efficiency over core-loss EELS if it showed depth discrimination in SCEELM. However, the preservation of elastic contrast in the low-loss images could dominate the pure inelastic contrast for confocal applications; that is, the valence-loss SCEELM (VL-SCEELM) may potentially retain the missing-information-cone problem (Howie, 1963; Muller & Silcox, 1995). In this paper, we demonstrate, both theoretically and experimentally, that the missing-information cone can be filled for VL-SCEELM. We also show that the 3D CTF and the depth resolution are sensitive to the size of rejection pinhole, which to date has not been studied systematically. Ultimately, the depth resolution is limited by the STEM depth of focus and the delocalization of inelastic scattering. With the aid of a C_c corrector, VL-SCEELM can potentially enable rapid 3D reconstruction of objects with sub-10-nm resolution with a dose efficiency for each single-image acquisition at different defoci comparable to that of STEM-EELS.

The remainder of this paper is organized as follows. First, we review the theory of SCEELM. Then, we show the 3D CTF of SCEELM as a function of energy loss and as a function of the pinhole size. Finally, we show the results of depth sectioning on a carbon thin film in C_c corrected SCEELM using valence-loss inelastic scattering.

THEORETICAL BACKGROUND

The Formalism of SCEELM

As a starting point and first approximation to the problem, we first consider the paraxial scattering and Born approximations, and ignore elastic scattering in the ingoing (elastic) and outgoing (inelastic) channels. The ideal SCEELM image (i.e., in which a vanishingly small pinhole is used) of a single atom can then be modeled as follows (see the online Supplementary Material for the derivation):

$$I(\mathbf{R}_p, \Delta f) = \sum_n \left| \int \varphi^*(\mathbf{R}, -\Delta f) V_{n0}(\mathbf{R} + \mathbf{R}_p) \psi_0(\mathbf{R}, \Delta f) d^2\mathbf{R} \right|^2, \quad (1)$$

where n labels the excited states of the atom; $\mathbf{R} = (x, y)$ is a 2D vector transverse to the optic axis; \mathbf{R}_p is the transverse position of the electron beam with respect to the atom; Δf is the defocus of the prespecimen lens, which is matched by the postspecimen lens; $\psi_0(R, \Delta f)$ is the wave function of the ingoing beam in the plane of the atom; $\varphi(\mathbf{R}, -\Delta f)$ is the wave function of a “conjugate” beam that originates on the detector and is focused by the postspecimen lens; and $V_{n0}(\mathbf{R})$ is the projected matrix element (Batson, 1993; Dwyer, 2005) describing the inelastic transition:

$$V_{n0}(\mathbf{R}) = \iint \phi_n^*(\mathbf{r}') \frac{1}{|\mathbf{r} - \mathbf{r}'|} \phi_0(\mathbf{r}') d^3\mathbf{r}' e^{-i2\pi q_z z} dz, \quad (2)$$

where \mathbf{r} is the 3D vector; and

$$q_z \approx \frac{1}{\lambda} \frac{\Delta E}{E} \left(\frac{E + m_0 c^2}{E + 2m_0 c^2} \right) \\ = \left(\text{in low-energy limits } q_z \approx \frac{1}{\lambda} \frac{\Delta E}{2E} \right)$$

is the change of the wave vector due to the loss of energy, ΔE , of the incident electron of kinetic energy E , relativistic wavelength λ (m_0 is the electron rest mass and c the speed of light). In equation (2), ϕ_0 is the initial core electron wave function, and ϕ_n is an excited final state.

Supplementary Material

To view supplementary material for this article, please visit <http://dx.doi.org/10.1017/S1431927613001438>.

A Comparison of SCEELM with STEM-EELS under the Local Approximation

The formulation for SCEELM in equation (1) is almost the same as that for STEM-EELS except that the function $\psi(\mathbf{R}, -\Delta f)\psi^*(\mathbf{R}', -\Delta f)$ is in the place of the detector function $D(\mathbf{R} - \mathbf{R}')$:

$$I_{\text{STEM-EELS}}(\mathbf{R}_p, \Delta f) = \sum_n \iint [D(\mathbf{R} - \mathbf{R}') V_{n0}^*(\mathbf{R} + \mathbf{R}_p) \\ \times V_{n0}(\mathbf{R}' + \mathbf{R}_p) \psi_0^*(\mathbf{R}, \Delta f) \\ \times \psi_0(\mathbf{R}', \Delta f)] d^2\mathbf{R} d^2\mathbf{R}', \quad (3)$$

where the detector function for a regular on-axis collection aperture of reciprocal radius of β_{max} is

$$D(\mathbf{R}) = \int_0^{\beta_{\text{max}}} \exp[-i2\pi k_0 \boldsymbol{\theta} \cdot \mathbf{R}] d^2\boldsymbol{\theta}. \quad (4)$$

Unlike in SCEELM, the detector function in STEM-EELS is independent of the probe defocus. In SCEELM, the postspecimen lens creates an envelope function $\varphi(\mathbf{R}, -\Delta f)\varphi^*(\mathbf{R}', -\Delta f)$ around the focal point, which gives rise to the improved depth discrimination of SCEELM and a CTF without a missing-information cone. To elucidate this point, let us compare and contrast the point spread function (PSF) and k_z dependence of the CTF at $k_x = k_y = 0$ of STEM-EELS and SCEELM.

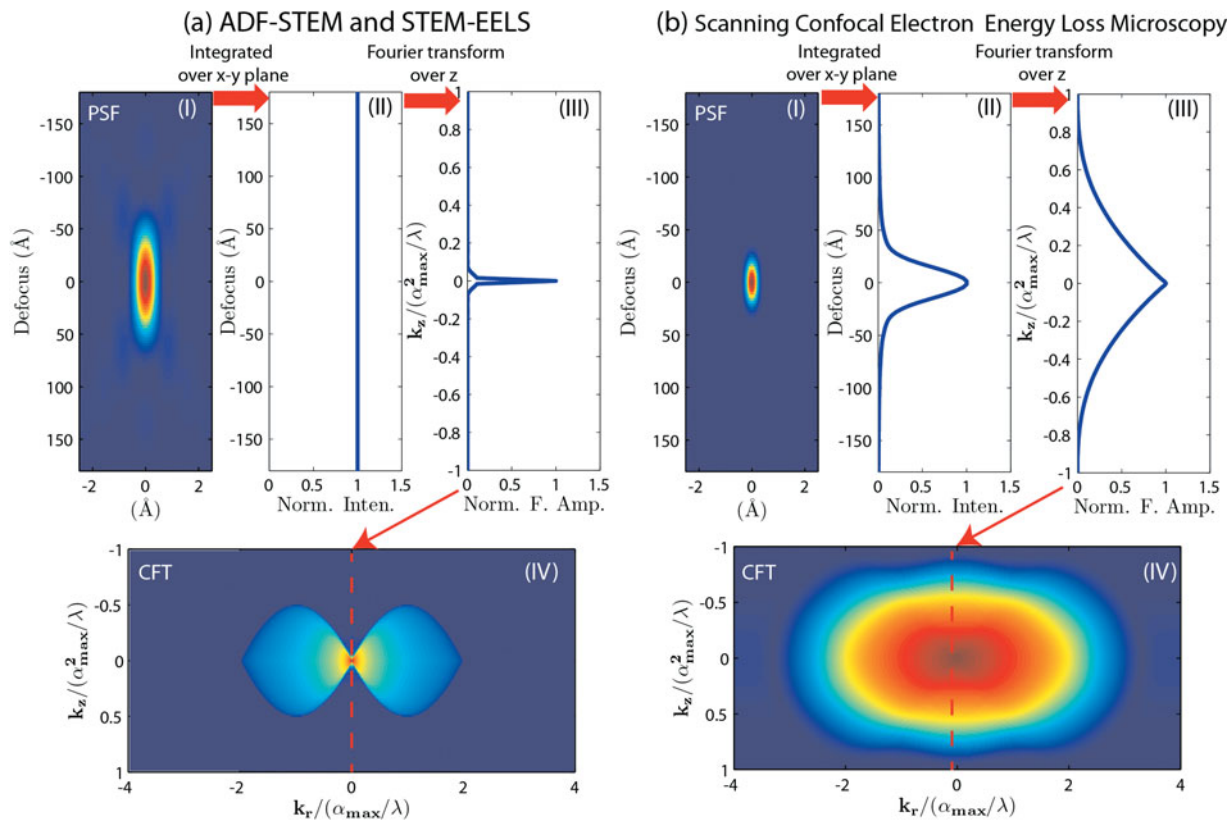


Figure 2. The comparison between scanning transmission electron microscopy-electron energy-loss spectroscopy (STEM-EELS) and scanning confocal electron energy-loss microscopy (SCEELM) with local approximation illustrating SCEELM's improvement in transferring low-frequency information near the reciprocal space origin ($E_0 = 80$ kV, $\alpha_{\max} = 30$ mrad, aberration free. For SCEELM, $\beta_{\max} = 30$ mrad). **a:** Point spread function (PSF) and contrast transfer function (CTF) for annular dark-field-STEM and STEM-EELS with local approximation. **b:** PSF and CTF for SCEELM with local approximation. (I) The cross-section of the 3D PSF; (II) the depth profile function, that is, the PSF integrated over the x - y plane; (III) the Fourier transform of the depth profile function, that is, the profile across $k_r = 0$ in the (IV) CTF.

For simplicity and before considering the more general case, we will first assume that the inelastic scattering is fully local, that is, $V_{n0}(\mathbf{R}) = \delta(\mathbf{R})$. For STEM-EELS, we will also assume that all of the scattered electrons are collected, so that $D(\mathbf{R} - \mathbf{R}') = \delta(\mathbf{R} - \mathbf{R}')$. In this case, the PSF of STEM-EELS is

$$I_{\text{STEM-EELS}}(\mathbf{R}_p, \Delta f) = |\psi_0(\mathbf{R}_p, \Delta f)|^2. \quad (5)$$

With the local approximation, the STEM-EELS PSF is the 3D intensity profile of a convergent electron beam. As the number of electrons is conserved in a propagating convergent beam, the total intensity of the PSF at every defocus, $\int |\psi_0(\mathbf{R}, \Delta f)|^2 d^2\mathbf{R}$, is a constant independent of defocus [Fig. 2a(II)]. Therefore, the depth frequency response at $k_x = 0, k_y = 0$ for STEM-EELS is a delta function:

$$\begin{aligned} \text{CTF}_{\text{STEM-EELS}}(k_x = 0, k_y = 0, k_z) &= \int |\psi_0(\mathbf{R}, \Delta f)|^2 d^2\mathbf{R} e^{-i2\pi k_z \Delta f} d\Delta f \\ &= \text{constant} \times \int e^{-i2\pi k_z \Delta f} d\Delta f \\ &= \text{constant} \times \delta(k_z). \end{aligned} \quad (6)$$

The resultant Dirac delta function shows that STEM-EELS along ($k_x = 0, k_y = 0$) does not transfer information except at $k_z = 0$, which is a manifestation of the missing-information cone [Fig. 2a(III, IV)].

For SCEELM, we obtain the PSF as

$$I_{\text{SCEELM}}(\mathbf{R}_p, \Delta f) = |\varphi(\mathbf{R}_p, -\Delta f)|^2 |\psi_0(\mathbf{R}_p, \Delta f)|^2. \quad (7)$$

In contrast to STEM-EELS, the SCEELM PSF is a product of the 3D intensity profile of two convergent electron beams, one from the prespecimen optics and one from the postspecimen optics. Because of the multiplicative superposition, the integrated intensity of the SCEELM PSF at each defocus, $\int |\varphi(\mathbf{R}, -\Delta f)|^2 |\psi_0(\mathbf{R}, \Delta f)|^2 d^2\mathbf{R}$, varies with defocus. This property is shown in Figure 2b(II), which is the numerically integrated profile of the PSF over the x - y plane. The $\text{CTF}_{\text{SCEELM}}(k_x = 0, k_y = 0, k_z)$ is shown in Figure 2b(III), which is the Fourier transform of the depth profile function, that is, $\int |\varphi(\mathbf{R}, -\Delta f)|^2 |\psi_0(\mathbf{R}, \Delta f)|^2 e^{-i2\pi k_z \Delta f} d^2\mathbf{R} d\Delta f$. It shows that SCEELM, unlike STEM-EELS, transfers information at finite k_z around ($k_x = 0, k_y = 0$). The missing-information cone present in ADF-STEM, STEM-EELS, and BF-STEM is eliminated in SCEELM allowing for simple 3D reconstruction of objects from energy-loss signals.

Delocalization

SCEELM images are also dependent on delocalization of inelastic scattering, that is, the transition potential $V_{n0}(\mathbf{R})$. As shown in equation (1), $V_{n0}(\mathbf{R})$ can be considered the “object” function of a single atom for a certain transition. Inelastic scattering of low-energy excitations is a delocalized process (Rose, 1976a, 1976b; Kohl & Rose, 1985); the “object” is therefore extended, but finite in size. The fundamental resolution limit of SCEELM is the spatial extent of the “object.” Most previous studies have only focused on high-energy excitations due to better localization and ultimate spatial resolution, where the local approximation is more closely satisfied (D’Alfonso et al., 2008). To understand valence-loss SCEELM, we need to calculate the “object” function for lower-lying excitations.

In simple metals, collective excitations, such as volume and surface plasmons, dominate the valence-loss spectra. In this case, Thomas–Fermi screening length, $1/\sqrt{me^2k_f/\epsilon_0\pi^2\hbar^2}$ (k_f is the Fermi wave vector), is part of the “object” size or the scale of the impulse response function. For example, for aluminum, copper, and gold, the Thomas–Fermi screening length is 0.49, 0.55, and 0.59 Å, respectively. In addition to this screening length, the other factor is the long-range Coulomb interaction between the incident electrons and the electrons in the metals. This delocalization, also known as the maximum impact parameter (b_{\max}), is energy-loss dependent— $b_{\max} = \gamma\hbar v/\Delta E = (1/2\pi q_z)((E + m_0c^2)/m_0c^2)$, where v is the velocity of the incident electron, γ is the Lorentz factor, ΔE is the energy loss, and q_z is the change in the wave vector. In addition, different modes of collective excitations are sample/beam geometry sensitive and therefore couples differently to the transverse and parallel time-varying electric field of the probing electron. The delocalization is also dependent on the probe forming and collection angles. The collective modes dominate at low scattering angles, but at angles larger than about half the first Bragg spacing the single-particle excitations dominate. In a corrected system, the latter is a significant fraction of the intensity and can be exploited.

For d - and f -electron systems, and isolated molecules, however, valence-loss spectra are usually dominated by interband transitions. Therefore, we can use equation (1) to model valence-loss SCEELM for these materials. This formulation includes the effects of the initial and final states, the long-range Coulomb interaction, and the probe-forming and collection geometries. In a simplification, we use the $1s \rightarrow 2p$ and $2p \rightarrow 3d$ transitions of a hydrogen atom to simulate the delocalization of the excitation process at energy losses of 10.2 and 1.9 eV, respectively. This hydrogenic approximation is applicable to a large class of interband transitions and should yield a good approximation of the ultimate spatial resolution of VL-SCEELM.

Figure 3 shows the transition potential for four selected transitions. As expected, the lower energy $2p \rightarrow 3d$ excitation is much more spatially delocalized than the $1s \rightarrow 2p$ excitations. If the $1s \rightarrow 2p$ (10.2 eV) transitions for p_x , p_y ,

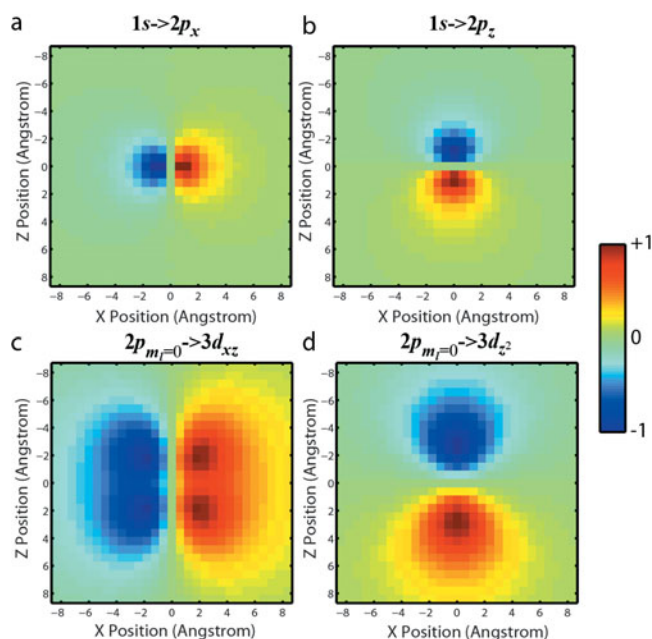


Figure 3. The inelastic transition potential for hydrogenic excitations (a) $1s \rightarrow 2p_x$, (b) $1s \rightarrow 2p_z$, (c) $2p_{m_l=0} \rightarrow 3d_{xz}$, (d) $2p_{m_l=0} \rightarrow 3d_{z^2}$.

and p_z are combined, the full-width at half-maximum (FWHM) of the transition is ≈ 0.4 nm in both the lateral and vertical dimensions. For the $2p \rightarrow 3d$ transitions, the FWHM is ≈ 1.2 nm. The maximum value provides an estimate of the “object” size of the lower-lying excitations. The result means that the fundamental resolution limit for VL-SCEELM is ~ 1 – 2 nm for low-loss signals dominated by $np \rightarrow nd$ interband transitions.

Pinhole Size

In the theoretical analysis of SCEELM presented above, we have assumed that the pinhole used to reject out-of-focus electrons is vanishingly small, that is, only a point detector is used to collect the SCEELM signal. A small pinhole provides maximum depth discrimination for SCEELM, but in practice a compromise must be made for the acquisition of finite signals. Therefore, the size of the pinhole is a degree of freedom in practical SCEELM. When the pinhole size is vanishingly small, it is the ideal confocal geometry, but no signals can be collected. On the other extreme, the pinhole may be so large as to collect all incident electrons, essentially reducing SCEELM to STEM-EELS. This reduction can be rigorously proved by Parseval’s theorem, which states that the sum of the squares of a function in real space is equal to the sum of the squares in reciprocal space. Large-pinhole SCEELM signals are collected as an image of the probe in real space, and STEM-EELS is collected in reciprocal space. Therefore, SCEELM without a pinhole is equivalent to STEM-EELS with a collection aperture equal to that of the postspecimen objective aperture size of SCEELM. Thus, the achievement of a sufficient signal-to-noise ratio at each scanned position while preserving depth discrimination requires a tradeoff between the pinhole size and the

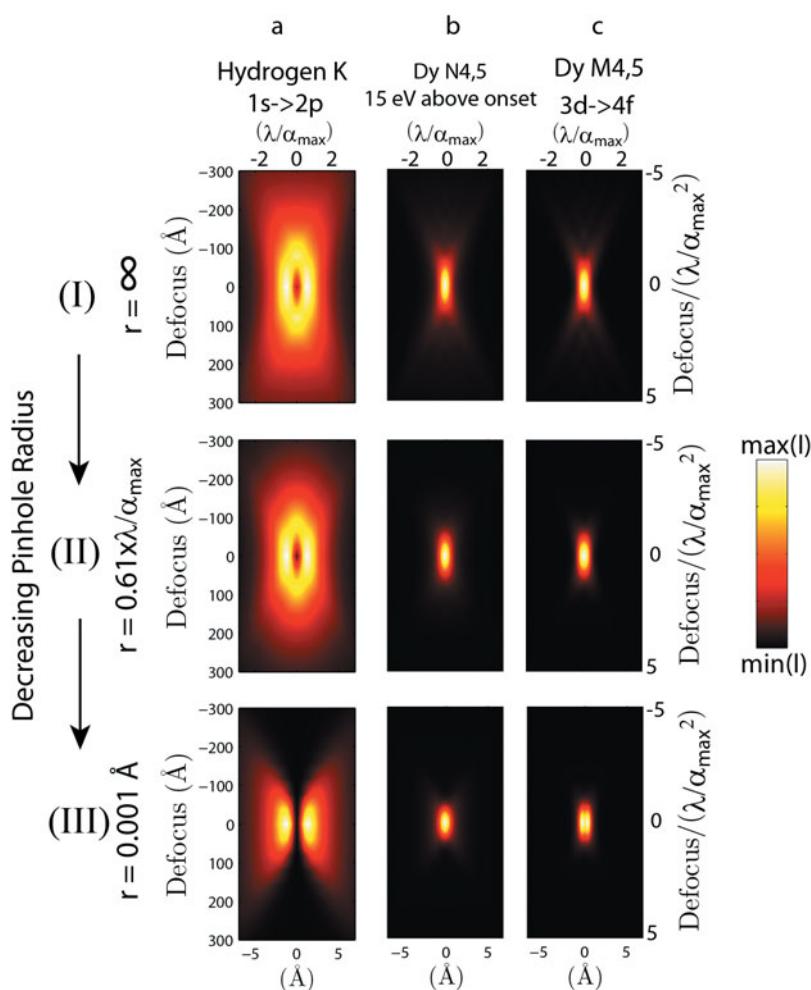


Figure 4. Pinhole-dependent scanning confocal electron energy-loss microscopy (SCEELM) 3D point spread functions of single atoms using (a) valence- and (b,c) core-loss excitations. The displayed PSF cross-sections are from full multi-pole calculations of the SCEELM depth sectioning of single atoms using the (a) hydrogen $1s \rightarrow 2p$ transition, the (b) Dy $N_{4,5}$ edges ($4d \rightarrow \text{continuum}$ 15 eV above onset), and the (c) Dy $M_{4,5}$ edges ($3d \rightarrow 4f$ white line). (The SCEELM imaging condition was $E_0 = 80$ keV, $\alpha_{\max} = 30$ mrad, $\beta_{\max} = 30$ mrad.) The pinhole size decreases from top to bottom.

signal collection. In the next section, we will use simulations to explore the pinhole and delocalization effect systematically.

SCEELM SIMULATION: CTF, PSF, AND DSF

Delocalization sets the fundamental limit of spatial resolution for inelastic processes and is independent of the quality of the electron optics. In most STEMs, the practical resolution for SCEELM is limited by how well the optics can focus the electron beam. Uncorrected instruments are limited by third-order spherical aberration, and when equipped with the highest quality (low C_s) pole piece are generally operated with a 10 mrad semiangle probe-forming aperture to achieve 1.3–3 Å lateral resolution depending on incident beam energy. With aberration correction, probe-forming apertures can be increased to 20–30 mrad limited by the C_c of the focusing lenses and residual geometric aberrations. This $3\times$ increase in the numerical aperture leads to sub-Angström lateral resolution and sub-10-nm depth of focus. It was thought that the improved depth resolution would provide rapid focal-series reconstruction of extended objects; however, for ADF-STEM, STEM-EELS, and BF-STEM, the 3D CTF has a missing-information cone along the projection direction. The full beam still passes from the

source through the object to the detector regardless of the defocus, and the postspecimen lenses for these configurations have no mechanism for rejecting out-of-focus electrons. Many previous studies have formulated the 3D CTF of SCEELM using a local approximation, that is, the inelastic transition potential is a delta function, and showed that the missing-information cone can be filled up to $k_z = \alpha_{\max}^2/\lambda$ (Cosgriff et al., 2008; D'Alfonso et al., 2008; Xin & Muller, 2009, 2010). In studying SCEELM image formation, D'Alfonso et al. (2008) simulated the SCEELM PSFs, but the simulations were for core-loss edges only and no reciprocal space CTFs were calculated. To date, no SCEELM simulations have been published to show the delocalization-dependent filling of the missing-information cone in 3D CTFs, which is critical for the interpretation of 3D SCEELM reconstructions. Here, we provide the first comprehensive study that shows excitation-dependent filling of the missing-information cone for both core- and valence-loss signals.

To show that SCEELM is one way to fill in the missing-information cone, we simulated confocal depth sectioning of a single atom using the EELS hydrogen K, Dy $N_{4,5}$, and Dy $M_{4,5}$ edges. Figures 4 and 5 show the SCEELM depth-sectioning result (PSF and CTF) as a function of excitation and pinhole size. Two trends are seen immediately. The first trend is the pinhole-dependent filling of the

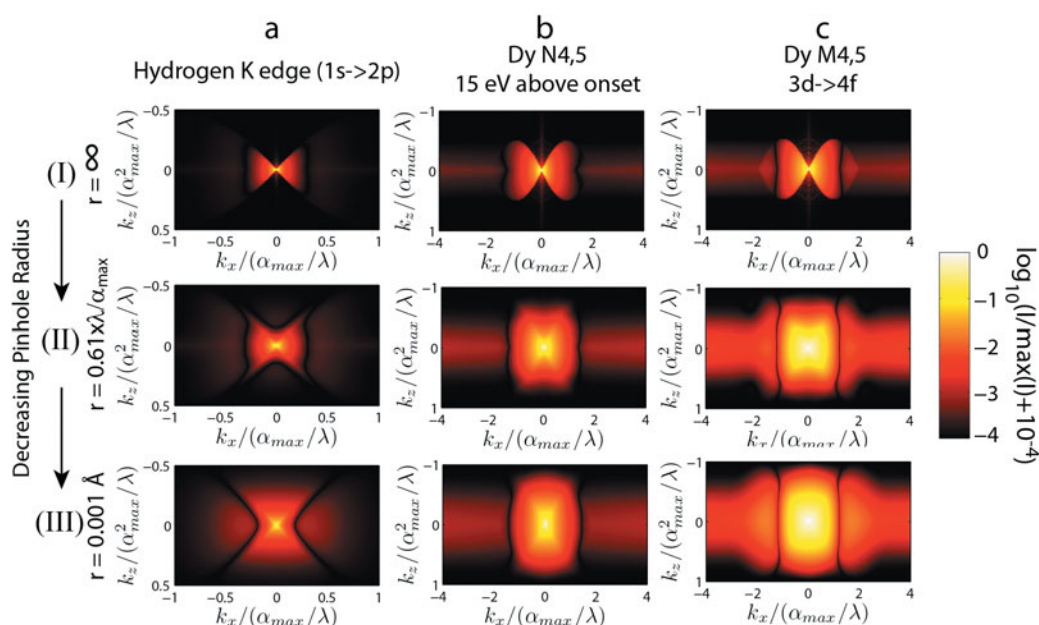


Figure 5. Pinhole-dependent scanning confocal electron energy-loss microscopy (SCEELM) 3D contrast transfer functions (CTFs) of single atoms using (a) valence and (b,c) core-loss excitations. The displayed CTF cross-sections are from full multi-pole calculations of the SCEELM depth sectioning of single atoms using the (a) hydrogen $1s \rightarrow 2p$ transition, the (b) Dy $N_{4,5}$ edges ($4d \rightarrow \text{continuum}$ 15 eV above onset), and the (c) Dy $M_{4,5}$ edges ($3d \rightarrow 4f$ white line). (The SCEELM imaging condition was 80 keV, $\alpha_{\text{max}} = 30$ mrad, $\beta_{\text{max}} = 30$ mrad.) The pinhole size decreases from top to bottom. Note that the lateral and vertical axis limits in (a) are reduced from those in (b) and (c).

missing-information cone. When the pinhole is large enough to collect the entire beam [Fig. 5(I)], SCEELM is reduced to STEM-EELS and the cross-section of the 3D CTF resembles airplane propeller blades with a missing-information cone along the beam axis. However, when the pinhole radius is reduced to $0.61 \times \lambda / \alpha_{\text{max}}$ [Fig. 5(II)], the missing-information cone is partially filled. (In this section, we assume a symmetric optical geometry, that is, $\alpha_{\text{max}} = \beta_{\text{max}} = 30$ mrad.) The information transfer is extended even further when the pinhole radius decreases to 0.001 \AA [Fig. 5(III)].

The second trend is horizontal across Figures 4 and 5 depicting the excitation-dependent delocalization effect. In real space, the dimension of the SCEELM PSF reduces both laterally and depth wise as higher-energy EELS excitations are used (Fig. 4). In reciprocal space, the limit of the lateral information transfer for the Dy $M_{4,5}$ edges is much larger than those for the Dy $N_{4,5}$ edges and hydrogen K edge because of transition-dependent delocalization. It is worth noting that even though the lobe of the hydrogen K CTF reaches its first minimum at $k_x \sim 0.25 \times \alpha_{\text{max}} / \lambda = (1/5.56) \text{ \AA}^{-1}$ [Fig. 5a(I)], the information transfer beyond that is nonzero. As for the depth information transfer, the boundary of transfer is not significantly different for the two Dy excitations. This is because the 6-nm depth of focus is much larger than the transition potentials for these two excitations (Dy-M and Dy-N). In the case of hydrogen K edge, the information transfer is certainly limited by the 4-\AA $1s \rightarrow 2p$ transition potential as shown in Figure 3. However, in Figure 5a(III), we see information transfer at $k_z = 0.5 \times \alpha_{\text{max}}^2 / \lambda = (1/92.8) \text{ \AA}^{-1}$. This demonstrates that achieving

sub-10-nm resolution using lower-lying EELS edges ($\Delta E > 10 \text{ eV}$) is possible in SCEELM.

Figure 6 shows the depth discrimination ability of SCEELM by integrating the simulated hydrogen K, Dy $M_{4,5}$, and $N_{4,5}$ signals in Figure 4 in the x - y plane. The curves presented are equivalent to the depth spread function (DSF) for a one atomic-layer-thick, infinitely wide membrane with different pinhole sizes and is the most pessimistic estimate of depth resolution (finite objects have finite elongation factors, even in the worst case). The yellow dashed line shows the variation in signal for an infinitely large pinhole, essentially STEM-EELS, and is independent of depth as expected. As the pinhole size decreases, the integrated signal becomes directly dependent on the defocus value. Figure 6g shows the FWHM of the DSF as a function of pinhole size. It shows that the FWHM increases nearly exponentially as the pinhole radius increases linearly. This shows the sensitivity of the pinhole size in rejecting out-of-focus electrons.

Delocalization of the inelastic transition is also manifested in these simulations, because the DSFs of the two Dy edges and the hydrogen K edge are much wider than that of the local approximation where the transition potential is assumed to be a delta function. In addition, the depth profiles of Dy-N (Fig. 6c) are much wider than those of Dy-M (Fig. 6f), whereas those of hydrogen K (Fig. 6b) are much wider than Dy-N (Fig. 6c), all in agreement with the expected delocalization. Figure 7h quantifies this phenomenon. It shows the DSF FWHM reduces with increasing energy loss, and at high energy losses the FWHM approaches the local approximation limit set by the depth of

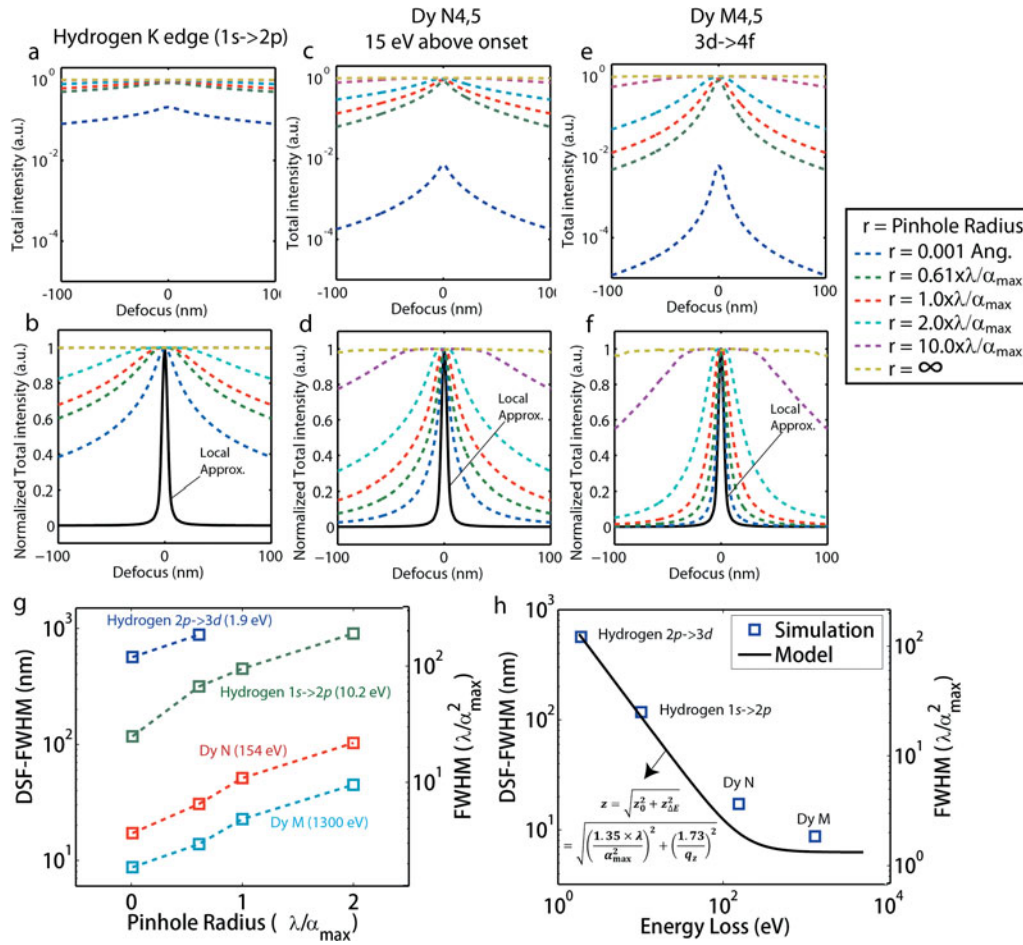


Figure 6. The depth profile of the 3D point spread function integrated on the x - y plane [scanning confocal electron energy-loss microscopy depth spread function (DSF)] of the (a,b) hydrogen $1s \rightarrow 2p$ transition, the (c,d) Dy N_{4,5} edges ($4d \rightarrow 15$ eV above onset *continuum*), and the (c,d) Dy M_{4,5} edges ($3d \rightarrow 4f$ white line) as a function of the pinhole radius. a, c, e: The depth profile on an absolute scale. b, d, f: The depth profile normalized by the peak intensity. Here the local approximation assumes the inelastic scattering potential is a 3D delta-function. g: The full-width at half-maximum (FWHM) of the DSF as a function of energy loss overlaid with the theoretically fitted model. h: The FWHM of the DSF as a function of pinhole size.

focus. Therefore, the DSF FWHM can be approximately modeled as an addition of the depth-of-focus-dependent part with the delocalization-dependent part in quadrature, that is:

$$z_{\text{DSF}} = \sqrt{z_0^2 + z_{\Delta E}^2} = \sqrt{\left(\alpha \times \frac{\lambda}{\alpha_{\max}^2}\right)^2 + \left(\frac{b}{q_z}\right)^2}. \quad (8)$$

Here, by least-square fitting, we determine the fitting parameters to be $a = 1.35$ and $b = 1.73$. The energy-loss-dependent DSF FWHM is therefore

$$z_{\text{DSF}} = \sqrt{\left(1.35 \times \frac{\lambda}{\alpha_{\max}^2}\right)^2 + \left(1.73 \times \frac{\lambda E}{\Delta E} \left(\frac{E + 2m_0 c^2}{E + m_0 c^2}\right)\right)^2}. \quad (9)$$

Therefore, the *depth* information in the missing-information cone along $k_x = k_y = 0$ is approximately transferred up to

$$k_z(k_x = k_y = 0)$$

$$= \frac{1}{z_{\text{DSF}}}$$

$$= \frac{1}{\sqrt{\left(1.35 \times \frac{\lambda}{\alpha_{\max}^2}\right)^2 + \left(1.73 \times \frac{\lambda E}{\Delta E} \left(\frac{E + 2m_0 c^2}{E + m_0 c^2}\right)\right)^2}}. \quad (10)$$

Equation (10) shows that information can be filled at the origin of the missing-information cone and it provides the most pessimistic estimate of the information transfer limits in the k_z direction. Note that, at finite $k_x = k_y \neq 0$, the transfer limits are larger.

It is worth mentioning that from equation (9) we see that once the depth of focus is smaller than the $1/q_z$, increasing the numerical aperture can only improve DSF FWHM by a maximum factor of 2. However, once the

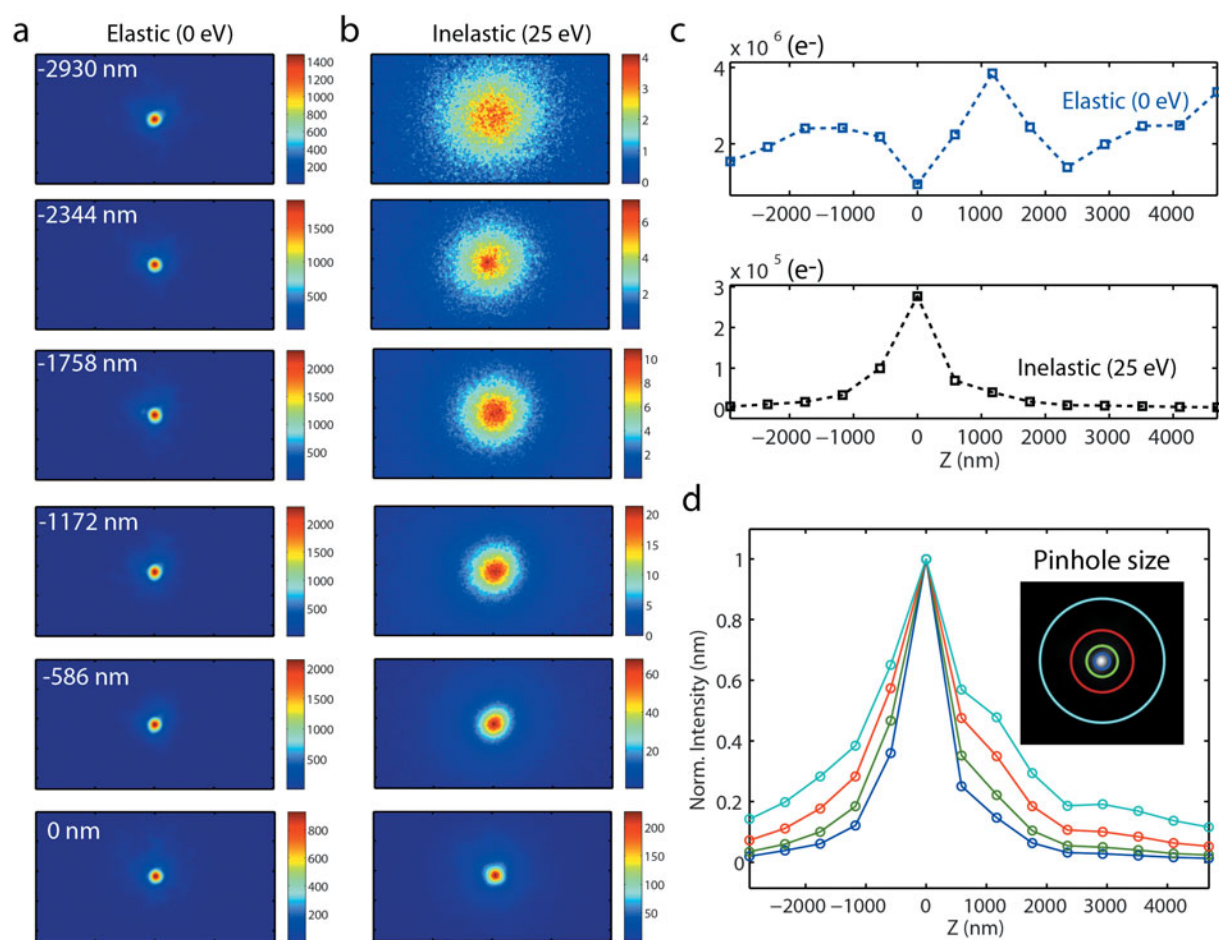


Figure 7. The energy-loss-dependent images of the 80-keV probe in serial scanning confocal electron energy-loss microscopy (energy-filtered mode) as the sample moves in and out of focus. Note the chosen z step size was much larger than the thickness of the carbon film. Therefore, the zero defocus is not necessarily the optimal focus; that is, neither the thickness of the film nor the depth resolution can be estimated from the profile in (c). (In (a), to same space, only images from the negative z positions are shown.)

probe is smaller than the impulse response function, depth resolution starts to be limited by delocalization. Consequently, a large numerical aperture has less benefit for the more delocalized low-loss signal compared with the localized high-energy-loss signals, where it can significantly improve the depth resolution.

THE SCEELM EXPERIMENT

Materials and Methods

We performed SCEELM experiments on the TEAM I double-corrected FEI Titan at the National Center for Electron Microscopy of Lawrence Berkeley National Laboratory. This instrument is fitted with a postspecimen CCOR chromatic-aberration corrector allowing both serial and parallel SCEELM experiments. We used both 80 and 300 keV incident beam energies, and the measured C_c was $-23.6 \mu\text{m}$ at 300 kV. The semiangle of the probe-forming aperture (α_{max}) was 17.7 and 30 mrad for 80 and 300 kV, respectively. No postspecimen objective aperture was used. The microscope is also equipped with a precision all-piezo-

driven sample stage that allowed true confocal geometry in which the defocus of the object was changed mechanically without variation of the electron optical conditions.

As a proof of concept, we used a holey C film as the test specimen. Because the material is translationally invariant in the lateral dimension, we only performed VL-SCEELM depth profiling of the material at a single (x, y) position. The condenser and objective lens excitations were kept unchanged during the data acquisition. The probing depth was changed by mechanically moving the piezo stage.

To study the energy-dependent delocalization and the pinhole-size effect of SCEELM, we performed the experiment both in energy-filtered mode (serial SCEELM) and in spectroscopy mode (parallel SCEELM). In the energy-filtered mode, with a 10-eV-wide energy-selecting slit, energy-filtered elastic and inelastic images of the probe were recorded with a Gatan imaging filter (GIF), and virtual pinholes of variable sizes were applied during postprocessing. In spectroscopy mode, the 1-mm-GIF entrance aperture was used as a physical pinhole and the C_c corrector allowed a large energy range of the spectrum to be simultaneously focused at the GIF.

Results

Serial SCEELM (Energy-Filtered Mode)

Figures 7a and 7b show the energy-filtered images of the elastic and inelastic ($20 \text{ eV} < \Delta E < 30 \text{ eV}$) exit waves as formed by the postspecimen lens and recorded with the same acquisition time. A dramatic difference between the two different sets of probe images is immediately evident. The probe in the elastic images remains constant in size independent of the relative separation between the sample and the electron beam focal point. However, the images of the electrons that lost $\Delta E = 25 \pm 5 \text{ eV}$ of energy spread out as the sample moves away from the focal point. This result reflects the fact that the low-loss signals used here are capable of forming depth-dependent probe images for pinholes to reject the out-of-focus blurs.

Figure 7c shows the BF-STEM (blue line) and low-loss SCEELM (black line) depth profiles extracted from Figures 5a and 5b by placing a digital pinhole as indicated by the blue circle in Figure 7d. The BF-STEM signal fluctuates up and down. An interpretation of the signal cannot be obtained directly, because both the amplitude and phase contrast of the carbon film are embedded in the BF-STEM images. However, the low-loss SCEELM profile has only a single peak, providing a directly interpretable depth-dependent signal for the localization of the carbon film. Figure 7d shows how the SCEELM depth profile varies with pinhole size, and as expected the profile widens as the pinhole widens. In addition, the peak SCEELM signal is approximately one-tenth of the full beam intensity for a 10-eV-wide energy window (Fig. 7c). This is comparable in cross-section to HAADF signals but with far superior depth-discrimination capability.

Figure 8 shows a second experiment carried out at 300 keV. In Figure 8a, the images of the probe at 0-, 25-, 50-, and 100-eV energy loss are recorded as a function of the sample z -height. The energy-dependent delocalization is directly visualized by the intensity of the out-of-focus images with nonzero energy loss. Figure 8b shows the two pinholes used to produce the profiles in Figure 8c. For either pinhole size, the elastic signal has a weak reverse contrast of the specimen. However, the inelastic signals each clearly show a single peak. The relative width of the peak increases as the energy loss decreases, reflecting the delocalization of low-energy excitations. It is also clear that the smaller pinhole size in Figure 8c produces improved depth discrimination compared with the large pinhole size.

Parallel SCEELM (Spectroscopy Mode + C_c Correction + Physical Pinhole)

Greater signal acquisition efficiency can be achieved by acquiring SCEELM signals at different energy losses in parallel. This requires a postspecimen C_c corrector to focus exit waves with different energies to the same image plane at the GIF. A physical pinhole is also needed to improve depth discrimination.

Figure 9a shows the image of an inelastic exit wave ($20 \text{ eV} < \Delta E < 30 \text{ eV}$) acquired with a rejection pinhole. A series of depth-dependent spectra can be acquired by using spectroscopy mode as shown in Figure 9b. Figure 9c shows the energy-loss-dependent depth profiles of the carbon film extracted from the spectra in Figure 9b. As the energy loss increases, the delocalization decreases, and the depth profile becomes narrower.

In principle, parallel SCEELM should work for both low- and core-loss signals. However, one must be cautious with background subtraction for lower-energy core edges, such as Si $L_{2,3}$. The sensitive energy dependency of SCEELM depth profiles poses a challenge for the correct estimation of the energy-dependent background.

DISCUSSION AND PERSPECTIVE

Scanning Mechanisms

A laterally translationally invariant thin film was used in this work. Scanning in the x - y plane was therefore not needed. However, mapping nanostructures in 3D requires a scanning mechanism in the x - y plane. Currently, a high-resolution piezoelectric stage-scanning system is available on TEAM I, and a similar system has been demonstrated to be suitable for STEM (Takeguchi et al., 2008; Hashimoto et al., 2009). However, as piezo stage scanning is not available in the vast majority of electron microscopes, it is much more attractive to improve postspecimen descanning in STEMs (Frigo et al., 2002). In principle, precise descanning is achievable with current technology, which would enable rapid acquisition of 3D SCEELM images with an electronic probe-scanning system interfaced to standard TEM/STEMs.

C_c Correction

As we demonstrated, the use of postspecimen C_c correction is key for the parallel acquisition of SCEELM signals. This procedure is especially important for core-loss applications because both the preedge and postedge spectral regions must be simultaneously in focus in order to estimate background and signal. However, for a simple VL-SCEELM application, a C_c correction is not required. Current-generation C_c -correcting optics can simultaneously focus electrons across an energy range of 100 eV. However, when valence-loss and deep core-loss edges are simultaneously used, one needs to measure the C_c accurately and consider both the delocalization effect and the C_c -induced blurring at core-loss edges in the interpretation of the reconstructions.

Dedicated Imaging Mode, Alignment Procedures, and Residual Aberrations

In current instruments, there is no dedicated SCEELM imaging mode or alignment procedures. Users must set up a confocal geometry in STEM mode. In both our experiment and previous studies, threefold aberrations ($C_{2,3}$) are evident in the elastic images of the probe. Future alignment procedures incorporating wobbling of the corrector elements could help determine whether these residual aberrations

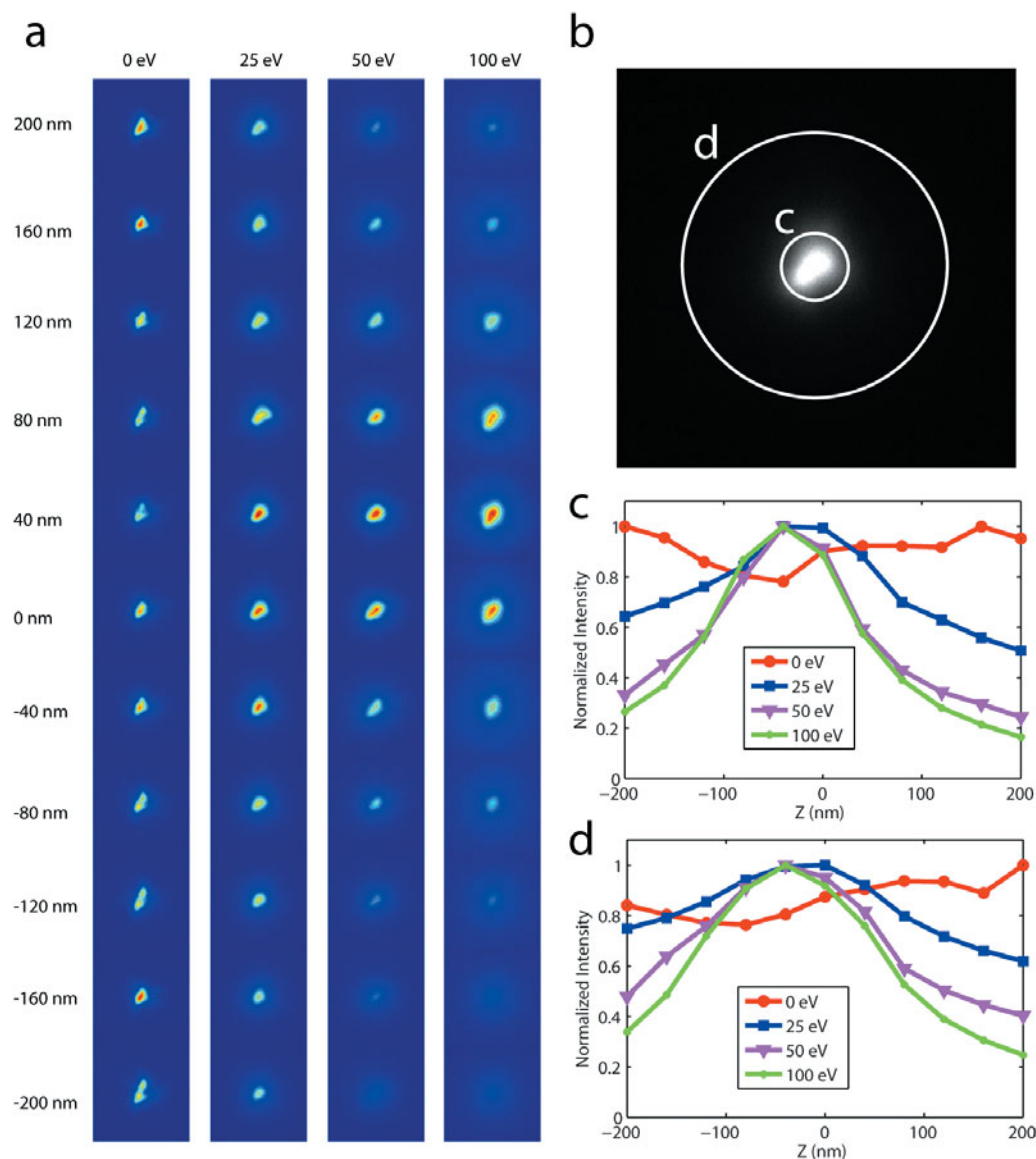


Figure 8. The energy-loss-dependent images of the 300-keV probe in serial scanning confocal electron energy-loss microscopy (energy-filtered mode) as the sample moves in and out of focus. **a:** The images of the probe as a function of the stage z position and the energy loss. **b:** The schematics showing the two chosen sizes of the digital pinholes. **c,d:** The energy-loss-dependent depth profiles of the carbon film.

tions are associated with the prespecimen optics or the postspecimen optics.

Depth Resolution, Deconvolution, and Combination with Tilt-Series Tomography

Without accounting for inelastic delocalization, the geometric depth of focus of SCEELM, assuming optimal lateral spatial resolution, is at a minimum the value of a diffraction-limited probe, λ/α_{\max}^2 . However, the depth resolution of SCEELM can be further limited by the C_c of the prespecimen probe-forming optics. Figure 10 plots the depth of focus of a 300 keV SCEELM as a function of the numerical aperture and the energy spread of the incident electron beam, assuming that the chromatic aberration coefficient of the probe-forming lens is 1 mm. This figure shows that a

1-nm depth resolution is achievable if the energy spread of the beam can be reduced to 0.1 eV or, alternatively, if the chromatic aberration coefficient of the probe-forming lens can be reduced to 100 μm . Under these conditions, the depth of focus of the beam would be better than the delocalization length for valence-loss excitations.

Deconvolution has been proven ineffective for ADF-STEM depth sectioning because a large cone of information is not transferred (Behan et al., 2009; Xin & Muller, 2009; Hovden et al., 2011; Lupini & de Jonge, 2011; Ramachandra & de Jonge, 2012). The lost information cannot be retrieved by deconvolution unless prior knowledge of the sample is available. However, SCEELM does not suffer from a missing-information cone. In this case, even a simple Wiener deconvolution can be very effective in improving contrast in the

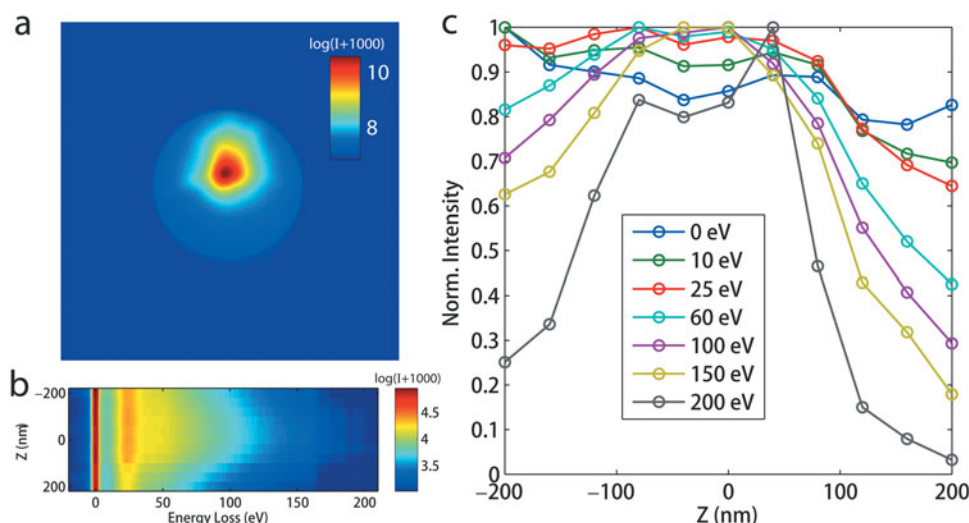


Figure 9. Parallel scanning confocal electron energy-loss microscopy (SCEELM) (spectroscopy mode + C_c correction + physical pinhole). **a:** The image of the probe and the pinhole. **b:** The depth-dependent SCEELM spectra. **c:** The energy-loss-dependent depth profiles of the carbon film extracted from the spectra in (b).

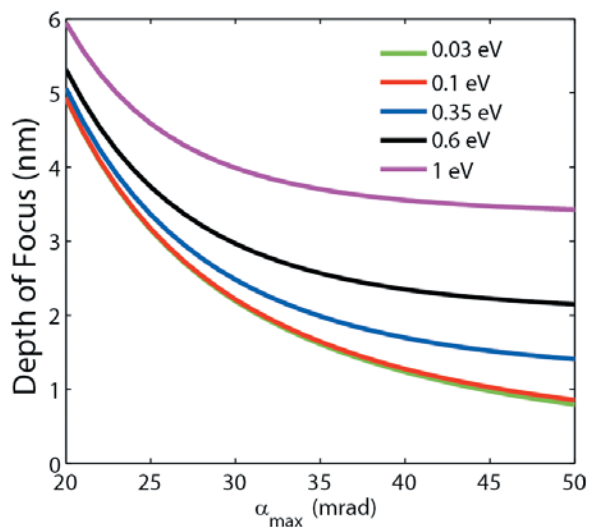


Figure 10. Depth of focus of 300 keV scanning confocal electron energy-loss microscopy as a function of numerical aperture and incident electron energy spread.

reconstruction. In addition, SCEELM reconstructions obtained from several tilt angles can be combined to improve the reconstruction resolution.

Acquisition Speed

The acquisition speed is limited by the spectrometer. In TEAM I, the Tridium GIF acquisition speed is limited to 10 spectra/s. However, with the newly developed quantum spectrometer, 1,000 spectra can be acquired per second. This speed allows a 128×128 -pixel parallel-SCEELM map to be recorded in 16 s assuming electronic (de)scanning. For a 100-nm object, assuming a 2-nm step size in z , a $128 \times 128 \times 50 \times 2,048$ through-focal SCEELM dataset can be acquired within 15 min. This is an order-of-magnitude improvement in acquisition speed over regular tilt-series

tomography, and 3D chemical information can be extracted from the dataset with minimal postprocessing. However, for VL-SCEELM applications with an energy slit, the acquisition time can be reduced to $10 \mu\text{s}$ (i.e., 100,000 spectra/s), but in this case the CCD readout speed is the limiting factor. As the signal is integrated anyway, a serial-EELS spectrometer using a single photomultiplier tube read-out can be used for such high-speed acquisitions.

Simulation of SCEELM Images

We note that in current theories (Dwyer, 2005; D'Alfonso et al., 2007), projected transition potentials are used for STEM-EELS and SCEELM simulations [equation (2)]; that is, the depth-dependent structure of the transition potentials are only partially considered. Such an approximation is clearly valid for conditions where the variation of the incident electron probe in depth is much slower than $1/q_z$, as is almost always the case for deep core-loss excitations. However, this condition can be violated in valence excitations when rapid channeling occurs, or when the depth of focus becomes smaller than the transition potentials. This is particularly relevant to the 1.9 eV hydrogen $2p \rightarrow 3d$ simulations—the size of the transition potential is 2 nm in z . If the depth of focus can be reduced to below 2 nm in future instruments, a more rigorous approach that does not invoke the projection approximation would be needed. For the present work, however, we anticipate that the projection approximation does not affect the results at the qualitative or semiquantitative level, and thus the conclusions of the present work are unaffected. The issue of the projection approximation with regard to the quantitative simulations of valence excitations will be considered further in future work.

In addition, the preservation of diffraction contrast in crystalline samples could potentially be a problem and likely will reduce the depth-dependent contrast by adding a

largely depth-invariant elastic background to the inelastic images, and should be checked for in future simulations and experiments.

CONCLUSION

In this paper, we have demonstrated both theoretically and experimentally that SCEELM using valence-loss excitations is free of the missing-information cone and the resulting elongation problem. As a function of the energy loss (ΔE) and the numerical aperture (α_{\max}), along $k_x = k_y = 0$, the missing information can be filled up to

$$k_z(k_x = k_y = 0) = \frac{1}{\sqrt{\left(1.35 \times \frac{\lambda}{\alpha_{\max}^2}\right)^2 + \left(1.73 \times \frac{\lambda E}{\Delta E} \left(\frac{E + 2m_0 c^2}{E + m_0 c^2}\right)\right)^2}},$$

giving a reduction of the elongation artifact and an increase to the contrast ratio of information at finite radial spatial frequencies $k_r \neq 0$. With proper chosen EELS excitations and numerical apertures, SCEELM is a promising technique for the reliable reconstruction of materials with sub-10-nm depth resolution. VL-SCEELM data acquisition is an order of magnitude faster and the postprocessing time is negligible compared with that of electron tomography. We also showed that postspecimen chromatic aberration (C_c) correction is critical for the wide application of SCEELM because of the ability to acquire multiple energy losses in parallel. Without the C_c correction, the postspecimen lens defocus needs to be adjusted for each individual energy loss, making it suitable only for valence-loss applications. Parallel VL-SCEELM has a dose efficiency comparable to that of ADF-STEM depth sectioning. With the C_c correction, SCEELM signals can be acquired in parallel in the energy-dispersive direction with the aid of a physical pinhole. The efficiency can be increased by $10\times$ to $100\times$, and chemical information can be extracted from simultaneously acquired core-loss edges.

ACKNOWLEDGMENTS

Research was supported by Materials Sciences Division, Lawrence Berkeley National Laboratory. Electron microscopy facilities in National Center for Electron Microscopy at Lawrence Berkeley National Laboratory was supported by the U.S. Department of Energy (DOE) under Contract #DE-AC02-05CH11231.

REFERENCES

BATSON, P.E. (1993). Symmetry-selected electron-energy-loss scattering in diamond. *Phys Rev Lett* **70**, 1822–1825.
 BATSON, P.E., DELLBY, N. & KRIVANEK, O.L. (2002). Sub-Angstrom resolution using aberration corrected electron optics. *Nature* **418**, 617–620.
 BEHAN, G., COSGRIFF, E.C., KIRKLAND, A.I. & NELLIST, P.D. (2009). Three-dimensional imaging by optical sectioning in the

aberration-corrected scanning transmission electron microscope. *Philos Trans R Soc London, Ser A* **367**, 3825–3844.
 BORN, M. & WOLF, E. (1999). *Principles of Optics: Electromagnetic Theory of Propagation, Interference and Diffraction of Light*. Cambridge, UK: Cambridge University Press.
 BOSMAN, M., KEAST, V., GARCÍA-MUÑOZ, J., D'ALFONSO, A., FINDLAY, S. & ALLEN, L. (2007). Two-dimensional mapping of chemical information at atomic resolution. *Phys Rev Lett* **99**, 086102.
 BOTTON, G.A., LAZAR, S. & DWYER, C. (2010). Elemental mapping at the atomic scale using low accelerating voltages. *Ultramicroscopy* **110**, 926–934.
 COSGRIFF, E.C., D'ALFONSO, A.J., ALLEN, L.J., FINDLAY, S.D., KIRKLAND, A.I. & NELLIST, P.D. (2008). Three-dimensional imaging in double aberration-corrected scanning confocal electron microscopy, part I: Elastic scattering. *Ultramicroscopy* **108**, 1558–1566.
 COUILLARD, M., RADTKE, G., KNIGHTS, A.P. & BOTTON, G.A. (2011). Three-dimensional atomic structure of metastable nanoclusters in doped semiconductors. *Phys Rev Lett* **107**, 186104.
 COX, I.J., SHEPPARD, C.J.R. & WILSON, T. (1982). Super-resolution by confocal fluorescent microscopy. *Optik (Stuttgart)* **60**, 391–396.
 D'ALFONSO, A.J., COSGRIFF, E.C., FINDLAY, S.D., BEHAN, G., KIRKLAND, A.I., NELLIST, P.D. & ALLEN, L.J. (2008). Three-dimensional imaging in double aberration-corrected scanning confocal electron microscopy, part II: Inelastic scattering. *Ultramicroscopy* **108**, 1567–1578.
 D'ALFONSO, A.J., FINDLAY, S.D., OXLEY, M.P., PENNYCOOK, S.J., VAN BENTHEM, K. & ALLEN, L.J. (2007). Depth sectioning in scanning transmission electron microscopy based on core-loss spectroscopy. *Ultramicroscopy* **108**, 17–28.
 DWYER, C. (2005). Multislice theory of fast electron scattering incorporating atomic inner-shell ionization. *Ultramicroscopy* **104**, 141–151.
 EINSPAHR, J.J. & VOYLES, P.M. (2006). Prospects for 3D, nanometer-resolution imaging by confocal STEM. *Ultramicroscopy* **106**, 1041–1052.
 ERCIUS, P., WEYLAND, M., MULLER, D.A. & GIGNAC, L.M. (2006). Three-dimensional imaging of nanovoids in copper interconnects using incoherent bright field tomography. *Appl Phys Lett* **88**, 243116.
 FRIGO, S.P., LEVINE, Z.H. & ZALUZEC, N.J. (2002). Submicron imaging of buried integrated circuit structures using scanning confocal electron microscopy. *Appl Phys Lett* **81**, 2112–2114.
 HASHIMOTO, A., MITSUISHI, K., SHIMOJO, M., ZHU, Y. & TAKEGUCHI, M. (2011). Experimental examination of the characteristics of bright-field scanning confocal electron microscopy images. *J Electron Microsc* **60**(3), 227–234.
 HASHIMOTO, A., SHIMOJO, M., MITSUISHI, K. & TAKEGUCHI, M. (2009). Three-dimensional imaging of carbon nanostructures by scanning confocal electron microscopy. *J Appl Phys* **106**, 086101.
 HASHIMOTO, A., WANG, P., SHIMOJO, M., MITSUISHI, K., NELLIST, P.D., KIRKLAND, A.I. & TAKEGUCHI, M. (2012). Three-dimensional analysis of nanoparticles on carbon support using aberration-corrected scanning confocal electron microscopy. *Appl Phys Lett* **101**, 253108.
 HOVDEN, R., XIN, H.L. & MULLER, D.A. (2011). Extended depth of field for high-resolution scanning transmission electron microscopy. *Microsc Microanal* **17**, 75–80.
 HOWIE, A. (1963). Inelastic scattering of electrons by crystals I. The theory of small-angle inelastic scattering. *Proc R Soc London, Ser A* **271**, 268–287.

- INTARAPRASONK, V., XIN, H.L. & MULLER, D.A. (2008). Analytic derivation of optimal imaging conditions for incoherent imaging in aberration-corrected electron microscopes. *Ultramicroscopy* **108**, 1454–1466.
- KOHL, H. & ROSE, H. (1985). Theory of image-formation by inelastically scattered electrons in the electron microscope. *Adv Electron El Phys* **65**, 173–227.
- KOURKOUTIS, L.F., XIN, H.L., HIGUCHI, T., HOTTA, Y., LEE, J.H., HIKITA, Y., SCHLOM, D.G., HWANG, H.Y. & MULLER, D.A. (2010). Atomic-resolution spectroscopic imaging of oxide interfaces. *Philos Mag* **90**, 4731–4749.
- KRIVANEK, O.L., NELLIST, P.D., DELLBY, N., MURFITT, M.F. & SZILAGYI, Z. (2003). Towards sub-0.5 Å electron beams. *Ultramicroscopy* **96**, 229–237.
- LI, H.Y., XIN, H.L., MULLER, D.A. & ESTROFF, L.A. (2009). Visualizing the 3D internal structure of calcite single crystals grown in agarose hydrogels. *Science* **326**, 1244–1247.
- LUPINI, A.R. & DE JONGE, N. (2011). The three-dimensional point spread function of aberration-corrected scanning transmission electron microscopy. *Microsc Microanal* **17**, 817–826.
- MIDGLEY, P.A. & DUNIN-BORKOWSKI, R.E. (2009). Electron tomography and holography in materials science. *Nat Mater* **8**, 271–280.
- MIDGLEY, P.A. & WEYLAND, M. (2003). 3D electron microscopy in the physical sciences: The development of Z-contrast and EFTEM tomography. *Ultramicroscopy* **96**, 413–431.
- MITSUISHI, K., HASHIMOTO, A., TAKEGUCHI, M., SHIMOJO, M. & ISHIZUKA, K. (2010). Imaging properties of bright-field and annular-dark-field scanning confocal electron microscopy. *Ultramicroscopy* **111**, 20–26.
- MULLER, D.A. (2009). Structure and bonding at the atomic scale by scanning transmission electron microscopy. *Nat Mater* **8**, 263–270.
- MULLER, D.A., KOURKOUTIS, L.F., MURFITT, M., SONG, J.H., HWANG, H.Y., SILCOX, J., DELLBY, N. & KRIVANEK, O.L. (2008). Atomic-scale chemical imaging of composition and bonding by aberration-corrected microscopy. *Science* **319**, 1073–1076.
- MULLER, D.A. & SILCOX, J. (1995). Delocalization in inelastic scattering. *Ultramicroscopy* **59**, 195–213.
- RAMACHANDRA, R. & DE JONGE, N. (2012). Optimized deconvolution for maximum axial resolution in three-dimensional aberration-corrected scanning transmission electron microscopy. *Microsc Microanal* **18**, 218–228.
- ROSE, H. (1976a). Image formation by inelastically scattered electrons in electron microscopy. *Optik (Stuttgart)* **45**, 139–158.
- ROSE, H. (1976b). Image formation by inelastically scattered electrons in electron microscopy II. *Optik (Stuttgart)* **45**, 187–208.
- SHEPPARD, C.J.R. (1986a). The spatial-frequency cutoffs in 3-dimensional imaging. *Optik* **72**, 131–133.
- SHEPPARD, C.J.R. (1986b). The spatial-frequency cutoffs in 3-dimensional imaging II. *Optik* **74**, 128–129.
- SHEPPARD, C.J.R. & CHOUDHURY, A. (1977). Image formation in the scanning microscope. *Optica Acta* **24**, 1051–1073.
- STREIBL, N. (1985). Three-dimensional imaging by a microscope. *J Opt Soc Am A* **2**, 121–127.
- TAKEGUCHI, M., HASHIMOTO, A., SHIMOJO, M., MITSUISHI, K. & FURUYA, K. (2008). Development of a stage-scanning system for high-resolution confocal STEM. *J Electron Microsc (Tokyo)* **57**, 123–127.
- TAN, H., TURNER, S., YÜCELEN, E., VERBEECK, J. & VAN TENDELOO, G. (2011). 2D atomic mapping of oxidation states in transition metal oxides by scanning transmission electron microscopy and electron energy-loss spectroscopy. *Phys Rev Lett* **107**, 107602.
- WANG, P., BEHAN, G., KIRKLAND, A.I., NELLIST, P.D., COSGRIFF, E.C., D'ALFONSO, A.J., MORGAN, A.J., ALLEN, L.J., HASHIMOTO, A. & TAKEGUCHI, M. (2011). Bright-field scanning confocal electron microscopy using a double aberration-corrected transmission electron microscope. *Ultramicroscopy* **111**(7), 877–886.
- WANG, P., BEHAN, G., TAKEGUCHI, M., HASHIMOTO, A., MITSUISHI, K., SHIMOJO, M., KIRKLAND, A.I. & NELLIST, P.D. (2010). Nano-scale energy-filtered scanning confocal electron microscopy using a double-aberration-corrected transmission electron microscope. *Phys Rev Lett* **104**, 200801.
- XIN, H.L., INTARAPRASONK, V. & MULLER, D.A. (2008a). Controlling channeling effects in aberration-corrected STEM tomography. *Microsc Microanal* **14**, 926–927.
- XIN, H.L., INTARAPRASONK, V. & MULLER, D.A. (2008b). Depth sectioning of individual dopant atoms with aberration-corrected scanning transmission electron microscopy. *Appl Phys Lett* **92**, 013125.
- XIN, H.L. & MULLER, D.A. (2009). Aberration-corrected ADF-STEM depth sectioning and prospects for reliable 3D imaging in S/TEM. *J Electron Microsc* **58**, 157–165.
- XIN, H.L. & MULLER, D.A. (2010). Three-dimensional imaging in aberration-corrected electron microscopes. *Microsc Microanal* **16**, 445–455.
- XIN, H.L., MUNDY, J.A., LIU, Z., CABEZAS, R., HOVDEN, R., KOURKOUTIS, L.F., ZHANG, J., SUBRAMANIAN, N.P., MAKHARIA, R., WAGNER, F.T. & MULLER, D.A. (2011). Atomic-resolution spectroscopic imaging of ensembles of nanocatalyst particles across the life of a fuel cell. *Nano Lett* **12**, 490–497.